Characterising micro-channel absorber plates for building integrated solar thermal collectors

Oyinlola, M.A [1*] and Shire, G.S.F [2].

[1]Institute of Energy and Sustainable Development, De Montfort University, Leicester, UK , LE 1 9BH

[2]School of Engineering, University of Warwick, Gibbet Hill Road, Coventry, UK, CV4 7AL

[*]Muyiwa.Oyinlola@dmu.ac.uk

Abstract.

This paper discusses the characterisation of micro-channel absorber plates for Compact Flat Plate solar thermal collectors. Experimental and computational studies were carried out at typical operating conditions for flat plate solar collectors; overall heat loss coefficient in the range 2 – 8 W/m^2.°C, flow rate in the range 0.01 – 0.1 kg/s/m^2 and heat transfer coefficients in the range 100 -1000 W/m^2.°C. Three Dimensional numerical analysis using commercial CFD package, Ansys CFX, showed that heat transfer occurred on only three surfaces of the channel and there was a peripheral variation of the heat flux density. It was also observed that axial thermal conduction could modify the surface boundary at the inlet and outlet, however, the middle section of the channel could be approximated as a rectangular channel with three walls transferring heat under a H1 boundary condition. Experimental studies were used to estimate the standard parameters (channel efficiency, *F*, collector efficiency factor, *F'*, heat removal factor, F_R, and flow factor *F")* for predicting performance of the flat plate collectors. An alternate parameter, channel efficiency, *F*, was proposed to replace Fin efficiency, *F*, used in standard collector analysis. The results showed that values of *F* and *F'*, very close to unity could be achieved with this design when the overall heat loss coefficient is below 2 W/m^2.°C. The analysis further revealed that increasing the fluid-plate heat transfer coefficient beyond 300 W/m^2.°C has marginal effect on the collector efficiency factor at a given U_L value. The collector flow factor *F"* and the heat removal factor could be improved by increasing the collector capacitance rate; this can be achieved by increasing the mass flow rate per collector area $\dot{m}/A_c$, as well as reducing the overall heat loss, U_L. This analysis is important for optimizing design and operating parameters, especially to minimize temperature gradient in the transverse and longitudinal directions.

Keywords: Micro-channel; Solar Absorber plate; Thermal Boundary; Heat transfer

Nomenclature

a	Channel depth (m)	h_E	Enthalpy (J/kg)
A_c	Channel flow area (m^2)	k	Thermal conductivity (W/m K)
A_p	Plate area (m^2)	k_f	Thermal conductivity of fluid (W/m K)
b	Channel width (m)	L	Length of channel (m)
CCR	Collector capacitance rate (-)	N_c	Number of channels in plate (-)
c_p	Specific heat capacity (J/kg K)	p	Pitch (m)
D_h	Hydraulic diameter (m)	P	Pumping power (W/m^2)
F	Fin Efficiency(-)	q	Heat flux density (W/m^2)
F'	Collector Efficiency Factor (-)	q_t	Heat flux on top of plate (W/m^2)
F''	F_R/F' (-)	Q	Heat supplied (W)
F_R	Heat Removal Factor (-)	S_c	Total surface area of channels (m^2)
h	Heat transfer coefficient (W/m^2 K)	SF	Shape Factor

S_E	Viscous work sources (kg/m s^3)
S_M	External momentum sources kg/m^2s^2)
T	Temperature (K)
t	Time (s)
T_f	Average fluid temperature (K)
T_{in}	Fluid temperature at inlet (K)
T_{out}	Fluid temperature at outlet (K)
T_p	Average plate temperature (K)
U	Vector of velocity
U_L	Overall heat loss coefficient (W/m^2 °C)
v	fluid velocity (m/s)
α	Aspect ratio (-)
δ	Identity matrix
$\dot{m}$	Mass flow rate (kg/s)
$\otimes$	Dyadic operator (tensor product)
∇	Gradient operator
ω	Uncertainty (-)
μ	Dynamic Viscosity (Pa.s)
Δp	Pressure drop (Pa)
ν	Kinematic viscosity (m^2/s)
ρ	Density (kg/m^3)
τ	Stress tensor

1. Introduction

Solar Thermal Flat Plate Collectors (FPCs) are often used as an environmentally friendly alternative to fossil fuel, in meeting the growing thermal energy demand in buildings. Significant progress has been made in improving the performance of these systems by various methods. For example, innovatively manipulating the geometry [1]-[4], improving heat transfer in the working fluid [5]-[7] and minimising the heat loss [8]-[11]. Several studies on building integrated FPCs have been carried out [12]-[14] however; the large size of these systems poses a challenge for aesthetically incorporating them in buildings. A viable option for building integrated FPC is a Compact (thin and light-weight) Flat Plate Collector (CFPC) [15], [16] . In this collector design, the absorber plate will have micro-channels that replace the conventional arrangement of tubes bonded to a metal sheet. Celata's [17] definition of a micro-channel as a channel whose hydraulic diameter lies between 1μm and 1 mm is adopted in this study. In addition to achieving the compact size, this design offers the advantage of enhanced convective heat transfer (based on the premise that the heat transfer coefficient is inversely proportional to the channel's hydraulic diameter), high fin efficiency, uniform temperature distribution in the transverse direction and eliminates the bond resistance between the tubes and absorber sheet in conventional FPC design.

A widely used method for characterising absorber plates of flat plate collectors is presented by Duffie and Beckman[18]. This method can however, be inadequate for characterising micro-channel absorber plates because heat transfer and fluid flow in micro- channels can differ from conventional theory due to scaling effects [19], [20]. For example, laminar heat transfer and fluid flow is usually analysed based on established Nusselt number correlations for idealised boundary conditions of constant wall temperature (CWT) and constant wall heat flux (CWH) conditions as outlined in Shah and London [21]. In micro-channels, however, it is difficult to achieve idealised boundaries because wall conduction has a strong influence on the temperature profiles, particularly at low Reynolds number [22], [23] and 3D conjugate heat transfer patterns in the solid and the fluid [24]. Therefore, applying an idealized surface boundary condition is likely to yield misleading results. Furthermore, in a solar collector, the heat to be dissipated will be incident on the top face of the plate; this will result in a peripheral variation of the heat flux density around the channel. Some scholars who investigated micro-channels subjected to a constant wall heat flux have assumed either a H1

(axially constant wall heat flux and circumferentially constant wall temperature) or H2 (uniform wall heat flux, axially, and circumferentially). For example Tunc and Bayazitoglu [25] used the H2 boundary condition while Lee and Garimella [26] suggested that H1 thermal boundary condition represents micro-channel heat sinks best. It is anticipated that the thermal boundary condition will fall between H1 and H2. Another difficulty can arise from many parallel micro-channels resulting in flow mal-distribution between the channels [27].

The need to propose a method for characterising micro-channel solar collector is further strengthened by the increased application of micro-channels to solar collectors. Some scholars who have applied micro-channels to solar collectors include Mansour [28]; who looked at flat plate rectangular channelled absorber plate, Sharma and Diaz [29]; who investigated its application in evacuated tube collector and Deng, et al. [30] who studied a novel FPC with micro-channel heat pipe array. Moss et al.[31] presented a method for identifying the optimum channel size based on pumping power limit. There is however no generalised method for analysing the design and operation of a micro-channel thermal collector. Another point worth noting is that using a conventional fin analysis will result in very high fin efficiency (above 0.995) which, does not necessarily indicate the heat sinking capabilities of the absorber plate.

This paper therefore proposes a method for characterising the performance of micro-channel solar collectors as well as uses a three dimensional modelling to propose the prevailing surface boundary condition in the channels. This analysis is important for the optimization of design and operating parameters, especially to minimize temperature gradient in the transverse and longitudinal directions. Minimizing temperature gradient on the absorber plate will improve collector's performance; collector's performance will be maximized if the whole absorber plate surface is at the same temperature as the inlet fluid [18].

2. Experimental Setup

2.1 Description of Experimental setup

The main difference between this collector and conventional FPC is the absorber plate. Therefore an experiment was set up to investigate the heat transfer and fluid flow behaviour of this absorber plate. The main component of the experimental setup was the micro-channel test rig which simulated the flat plate collector. Figure 1 is a picture of the inner surfaces of the test rig showing the micro-channels.

Figure 1: Micro-channel Test rig

Instruments to measure the temperature at different points, the pressure drop across the test rig and the mass flow rate were embedded at appropriate locations. Table 1 shows geometry details of the channels machined on the two plates used in this experiment. Temperatures of the plate at different points (T_{pi}), fluid at inlet (T_{in}) and fluid at outlet (T_{out}) were measured using Type T thermocouples. Several thermocouples were fixed on the absorber plate using fibre-glass thermal attachment pads. Figure 2 shows the thermocouple arrangement on the absorber plate. A comprehensive description of the experimental setup is presented in [19], [32].Table 2 shows how various parameters were estimated from the experiments

Table 1: Geometric parameters of the channels

Plate	***a* (mm)**	***b* (mm)**	***p* (mm)**	***D_h* (mm)**	***L* (mm)**	***α***	***N_c***
A	0.5	2	3	0.8	270	0.25	60
B	0.25	2	3	0.44	270	0.125	60

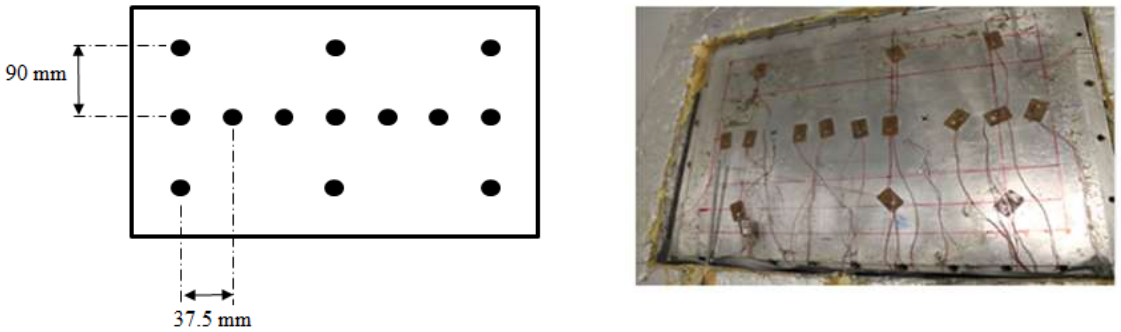

Figure 2: Thermocouple arrangement on micro-channel plate

Table 2: Data reduction

Parameter	**Definition**	**Equation number**	**Uncertainty**
Mean plate temperature	$T_p = \frac{\sum_{i=1}^{n} T_{pi}}{n}$	(1)	0.06°C

Mean fluid temperature	$T_f = \frac{T_{in} + T_{out}}{2}$	(2)	0.04°C
surface area of channels	$S_c = 2N_c L(a+b)$	(3)	0.00115m^2
Heat transferred to fluid	$Q = \dot{m}C_p\left(T_{out} - T_{in}\right)$	(4)	7W
Heat transfer coefficient	$h = \frac{Q}{S_c\left(T_p - T_f\right)}$	(5)	<20%
Pumping power per square meter	$P = \left(\frac{\dot{m}}{A_p}\right)\frac{\Delta p}{\rho}$	(6)	<10%

2.2 Convention

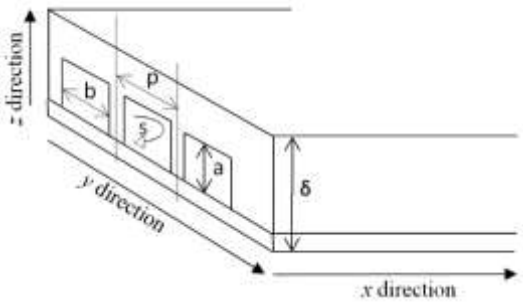

Figure 3: Description of micro-channel plate directions

Figure 3 describes the various directions in the micro-channel plate.

1. The fluid flows in the *x* direction, along the length (longitude) of the plate from inlet to outlet.
2. The channels are arranged in parallel along the width (transverse/y direction) of the plate from left to right.

Figure 4 shows the dimensions of the micro-channel absorber plate; channels have a depth *a*, width *b*, separated by a pitch distance *p*. The micro-channel plate has fluid passing along rectangular passages, the fourth side of the passage is formed by a cover plate that is clamped in place hard against the inter-passage ribs, and the plate has a total thickness *δ.*

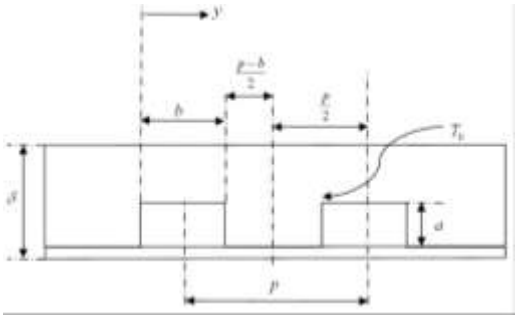

Figure 4: Micro-channel plate dimensions

3. Three Dimensional Modelling

Several studies focused on heat transfer and fluid flow in micro-channels have highlighted the importance of carrying out numerical investigation in conjunction with experimental studies. For example, Rosa et al [22] in a comprehensive review of heat transfer and fluid

flow in micro-channels, noted that for the case of heat exchangers with parallel micro-channels or when scaling effects are significant, correlations may only give a gross estimation of the Nusselt number hence suitable numerical simulations are necessary. Gamrat et al [33] stated that numerical modelling may be a very helpful tool to interpret experimental data, to test assumptions and may be also very useful to evaluate the relative importance of the physical phenomena possibly involved in micro-channel heat transfer. Fedorov and Viskanta [24] investigated conjugate heat transfer in a silicon heat sink with rectangular micro-channels. Their numerical and experimental results were in good agreement and they observed very complex heat flow patterns. They further showed that there is a very strong coupling between convection in the fluid and conduction in the silicon substrate that can only be resolved by a detailed three dimensional (3D) simulation. Lee et al [34] investigated heat transfer in 10 parallel rectangular micro-channels with hydraulic diameters ranging 0.3 – 0.9 mm and found that that the experimental results disagreed with all of the tested correlations but were well predicted by numerical simulations. This was attributed to the fact that 3D effects in the solid walls and fluid can significantly modify the thermal wall boundary condition in a heat exchanger with parallel channels. They recommended the use of numerical simulations with suitable boundary conditions, instead of correlations, to predict the performance of heat sinks using micro-channels.

In view of these, a 3D numerical simulation seems to be a pertinent part of investigating heat transfer and fluid flow in these micro-channel absorber plates. A numerical simulation has the potential to accurately predict the boundary conditions, measure the scaling effects and mal-distribution in the manifolds as well as address the 3D effects in the solid and fluid. Several commercial CFD software tools can be used to achieve this, for example, star CCM, Comsol, Fluent and CFX. This section presents details of the methods used in performing 3D numerical simulation on the micro-channel plates using a commercial CFD package - ANSYS CFX.

ANSYS CFX software is a high-performance, general purpose fluid dynamics program that has been applied to solve wide-ranging fluid flow problems for over 20 years [35] . The package uses the Navier–Stokes equations to describe the fundamental processes of momentum, heat, and mass transfer. The solver is highly parallelized and incorporates a number of mathematical models that can be used together with the Navier–Stokes equations to describe other physical or chemical processes such as turbulence, combustion, or radiation thus offering a wide range of physical models to capture virtually any type of phenomena related to fluid flow. This solver, like most commercial CFD packages, uses a finite volume approach; it integrates the conservation equations (equations (7),(8) and (9)) over all the control volumes in the region of interest i.e. applying a basic conservation law to each control volume.

Continuity

$$\frac{\partial \rho}{\partial t} + \nabla \bullet \left(\rho U_E \right) = 0 \qquad (7)$$

Momentum

$$\frac{\partial\left(\rho U_E\right)}{\partial t}+\nabla\bullet\left(\rho U_E\otimes U_E\right)=-\nabla p+\nabla\bullet\tau+S_M+S_E \tag{8}$$

Energy

$$\frac{\partial\rho h_{Etot}}{\partial t}-\frac{\partial\rho}{\partial t}+\nabla\bullet\left(\rho U_E h_{Etot}\right)=\nabla\bullet\left(k\nabla T\right)+\nabla\bullet\left(U_E\bullet\tau\right)+U_E\bullet S_M+S_E \tag{9}$$

Where

$$\tau=\mu\left(\nabla U_E+\left(\nabla U_E\right)^T-\frac{2}{3}\delta\nabla\bullet U_E\right)\qquad h_{Etot}=h_E+\frac{1}{2}U^2$$

The integral equations are then converted to a system of algebraic equations by generating a set of approximations for the terms in the integral equations [36]. The algebraic equations are solved iteratively (because of the non-linear nature of the equations), until it converges (approaches the exact solution). One of the most important features of CFX is that it uses a coupled solver, which solves the fluid flow and pressure as a single system and faster than the segregated solver up to a certain number of control volumes as it requires fewer iterations to achieve equally converged solutions[37].

This study is focussed on heat transfer and fluid flow therefore, a thermal energy model, which solves the energy transport equation, was used. The thermal energy model for the fluid is shown in equation (10), this model neglects variable density effects, however it is appropriate for the analysis as it is recommended for low speed liquid flows[36]. The model for heat transfer in the solid domain is presented in equation(11).

$$\underbrace{\frac{\partial\rho h_{Etot}}{\partial t}-\frac{\partial\rho}{\partial t}}_{Transient}+\underbrace{\nabla\bullet\left(\rho U_E h_{Etot}\right)}_{Convection}=\underbrace{\nabla\bullet\left(k\nabla T\right)}_{Conduction}+\underbrace{\nabla\bullet\left(U_E\bullet\tau\right)}_{viscouswork}+\underbrace{S_E}_{Sources} \tag{10}$$

$$\underbrace{\frac{\partial\left(\rho c_p T\right)}{\partial t}}_{Transient}=\underbrace{\nabla\bullet\left(k\nabla T\right)}_{Conduction}+\underbrace{S_E}_{Source} \tag{11}$$

As can be expected, this 20 year old solver has been used and validated by many, examples include [38]-[40]. However, for increased confidence, the simulation results from the CFD package was validated against experimental results. The procedure for performing the simulation is detailed below.

3.1 Geometry

The first step in a CFD simulation is to create a geometry that adequately represents the physical system to be studied. A geometry representing the experimental test rig was created with Ansys DesignModeller. This geometry consisted of four computational domains within which the equations of fluid flow and heat transfer were solved. The domains are the fluid, micro-channel plate, top slab and bottom slab. It should be noted that the two domains of interests are the fluid and micro-channel plate; however, the bottom and top slabs were included to have a geometry representing the experimental test rig. Figure 5a shows a wireframe of the whole geometry, it can be observed to be an exact replica of the actual test rig. Figure 5b shows the isolated fluid domain; it was created by filling the cavity between the micro-channel plate and the bottom slab. This can be seen to adequately represent fluid flow in the channels as well as the manifolds. The dimensions of the channel depth, width and pitch were set as workbench input design parameters to easily match the different plates.

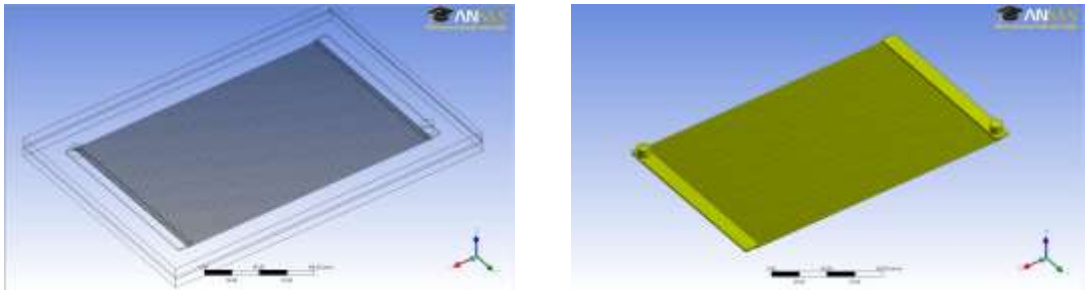

Figure 5: (a) Heated sandwich geometry (b) Fluid domain

3.2 Mesh

The next stage of the analysis is to discretise the domains into a number of small control volumes. This was done using the Ansys meshing program. Due to the small size of channel walls and plate thickness, unstructured grids consisting of tetrahedral, pyramid and prismatic elements, were employed. It is pertinent to carefully choose the mesh size so as to avoid adverse effect on the simulation accuracy, hence the quality of the mesh was checked in two ways. Firstly, mesh-associated parameters such as the edge length ratio, maximum and minimum face angle, connectivity number, and element volume ratio were checked [41]. Secondly, the influence of mesh size on the parameters of interest was checked. This was achieved by running simulations with differently refined meshes. It should be noted that the coarseness of the mesh for fluid and plate could not be more than half of the channel depth because the 3D simulation requires at least two mesh layers in a domain. Figure 6a shows the effect of the mesh size on the micro-channel plate domain by comparing the micro-channel plate temperature profile at different number of mesh nodes. It can be observed that the four finer meshes show mesh independent solutions (temperature varies by less than 0.1° at any given position) while the coarsest mesh can be observed to have a more significant difference (about 2 °C). The effect of mesh refinement on fluid temperature is shown in Figure 6b, the

temperature at any given position varies by less than 0.1°C which indicates a mesh independent solution for the fluid.

Table 3 gives details of meshes for the various domains; finer meshes were adopted for the domains of most importance (plate and fluid); a magnified and sectioned view the mesh in these domains can be seen in Figure 7. The mesh on the fluid domain in a few channels was made very fine, by using various mesh tools and controls. The boundary layer development on these few channels could be resolved and could be used as a representation for all channels.

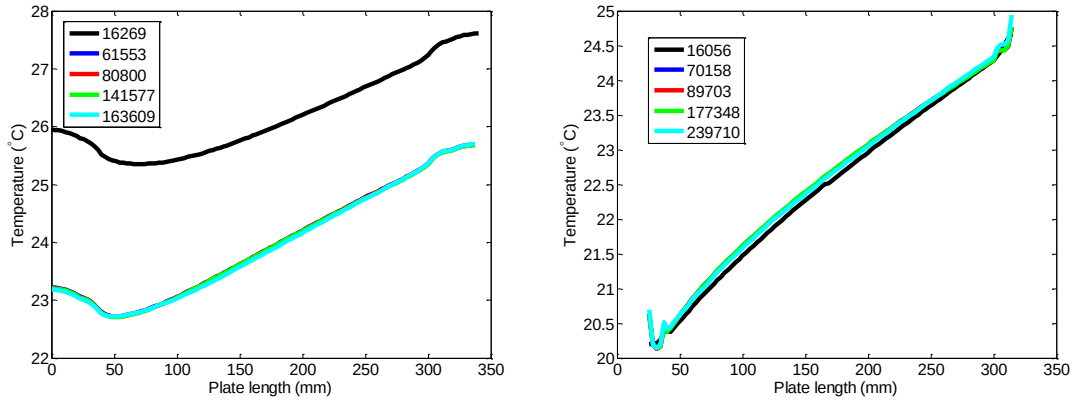

Figure 6: Temperature in flow direction at different number of nodes (a) Plate (b) Fluid

Table 3: Details of the mesh used

Domain	Nodes	Elements	Body Spacing	Min size	Curvature Normal Angle
Fluid	29968	811786	1.5 mm	0.1 mm	18 °
MC Plate	163989	654770	0.8 mm	0.1 mm	18 °
Top Slab	20984	15300	-	0.2 mm	18 °
Bottom Slab	29968	138149	-	0.2 mm	18 °
All Domains	454706	1620005			

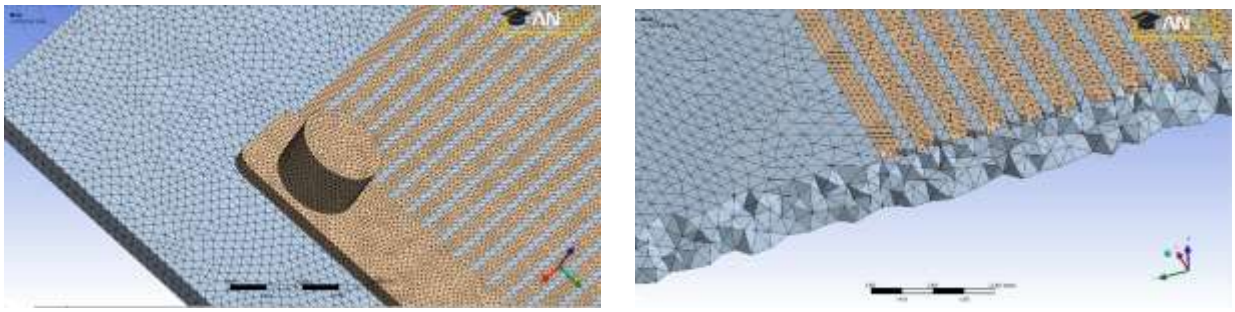

Figure 7: A magnified view of the mesh

3.3 Domain and boundary conditions

The next step of the simulation is to define the properties of the various domains and their corresponding boundary conditions. These were done to match actual experiments as much as possible however, some assumptions were made. These include

I. The flow is laminar and can be approximated as steady state.
II. Incompressible fluid flow.
III. Fluid properties are constant.
IV. Viscous dissipation, radiation and buoyancy are negligible.

Expressions for experimental variables were written using the CFX Expression Language (CEL). These expressions were then set as workbench input parameter which allowed experimental variables to be easily set. Since all experiments were run at very low flow rates (Re<100), no turbulence model was used. Appropriate interfaces were defined between domains

3.4 Simulation

After accurate definition of the domains and boundary conditions, simulations were run to match some of the experimental runs. Some of the precautions taken to ensure accurate solutions include

I. The solution no longer changes with subsequent iterations (checked by increasing the minimum number of iterations for different runs).
II. Overall mass, momentum, energy, and scalar balances are achieved (checked by viewing the solver monitor).
III. Setting the maximum residual to 10^{-6}
IV. Monitoring convergence using residual history.
V. Monitoring other relevant key variables/physical quantities for a confirmation.

One of the advantages of Ansys Workbench is the interactive post processing GUI that allows results of simulations to be thoroughly investigated. Most of the variables of interest such as heat flux, wall heat transfer coefficient, skin friction and fluid velocity for the whole domain are calculated and written to file. This allows the value of any of these variables at any point in the domain to be estimated. This is illustrated in Figure 8, which shows the CFD estimated temperature profile of the micro-channel plate. Temperature measurements can therefore be taken at the same location as temperature probes in the experiment thus making experimental and numerical results more comparable. Expressions and new variables can also be written using CEL. This was used to define parameters whose experimental and numerical values were to be compared; these variables were set as workbench output parameters. More representative quantities could be measured in CFX post, for example, the average fluid temperature can be estimated as the mass average fluid temperature using the built in

mathematical function *MassAve*, the average plate temperature can be estimated as the average temperature at the plate-fluid interface using the built in mathematical function *AreaAve* in conjunction with the 'location' function. It should be noted that the heat transfer coefficient written to file is the wall heat transfer coefficient i.e. the temperature difference between the plate – fluid interface and the adjacent fluid temperature. Therefore, an expression was written to estimate the average heat transfer coefficient from the mass averaged bulk fluid temperature and the average plate wall temperature.

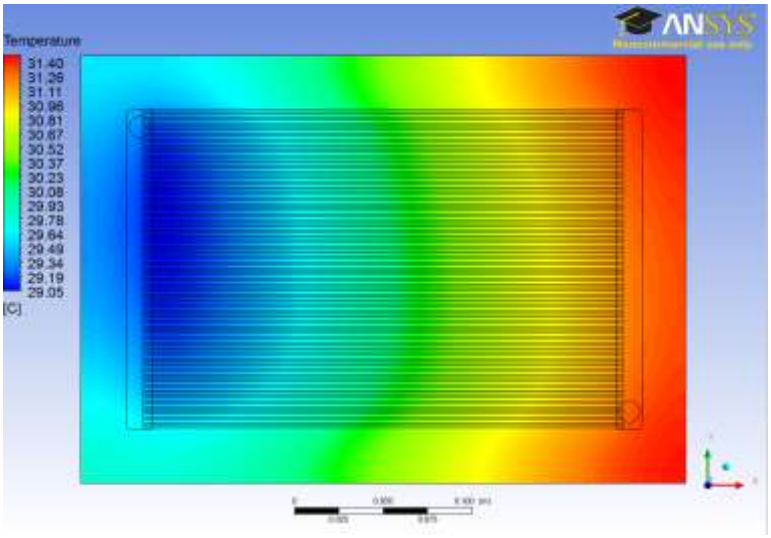

Figure 8: Plate temperature at the plate fluid interface

3.5 Validation with experimental results

Figure 9 shows a graph comparing the experimental and simulation results. Due to the difficulty of experimentally measuring the fluid temperature along the channel [42], only the inlet and outlet fluid temperatures are used. The curve from the numerical simulation intersects both inlet and outlet fluid temperatures, suggesting energy is conserved. The simulated plate temperature profile differs slightly from the experimental values; however, the difference is constant signifying that this might be an error resulting from uneven interface thickness in the experimental setup.

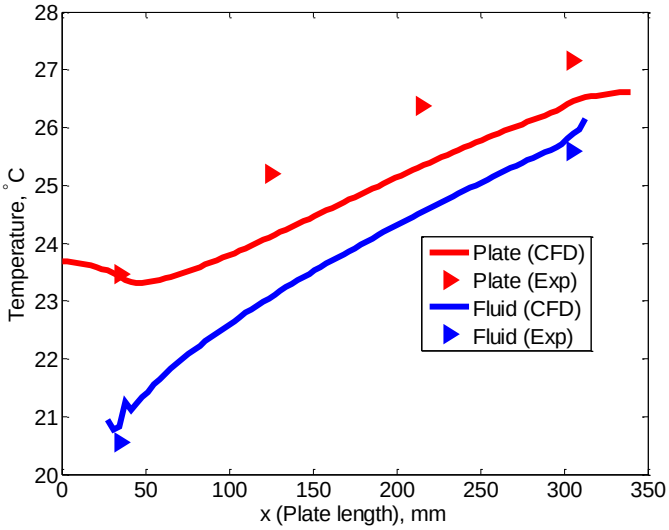

Figure 9: Comparing experimental and numerical results

4. Results and Discussion

4.1 Surface Boundary

To study the effects of conjugate heat transfer, a simulation was done on a plate with 500 mm long channels. Figure 10 shows the simulated axial temperature profile at the top surface and the middle of the fluid. A trend consistent with a constant temperature surface boundary condition is observed at the entry, while the middle section resembles a constant wall heat flux condition. The significance of axial thermal conduction will depend on several factors including the plate material and flow velocity, for example, a more conductive material and/or a lower flow velocity will yield more significant effects.

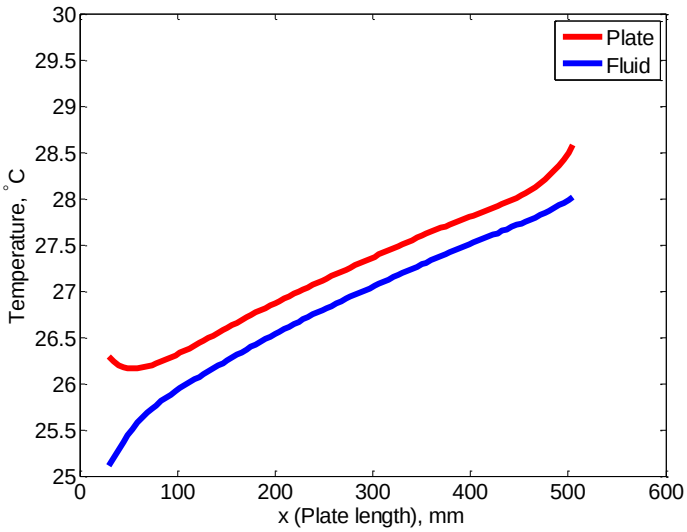

Figure 10: Simulated fluid and plate temperature profile

Figure 11 compares the axial surface temperature profile on the four walls; three walls (top and sides) can be observed to have approximately the same temperature profile while the fourth side differs by about 0.5 °C. This difference may be attributed to thermal contact resistance between the inter-passage ribs and cover plate (The channel is made by clamping a cover plate hard against inter-passage ribs of rectangular passages). This suggests that the surface boundary varies peripherally. It also indicates that the method of manufacturing the channel can significantly alter the surface boundary condition. Other methods of channel manufacture such as welding two hydro-formed sheets together (as required to prevent the plate ballooning under pressure/vacuum) should provide good thermal connection and promote a more uniform peripheral temperature.

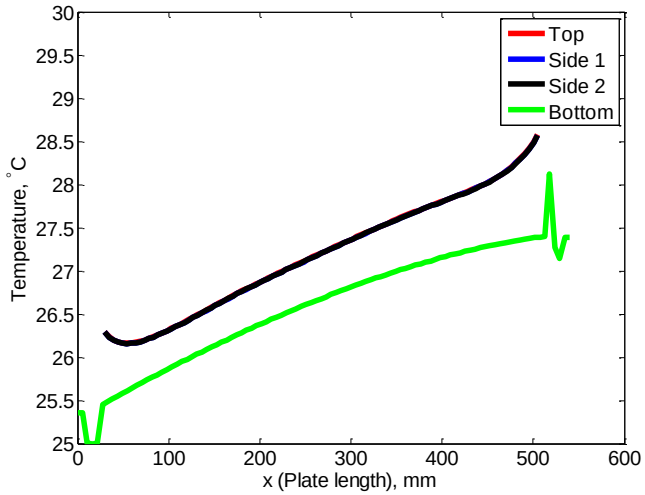

Figure 11: Temperature profile at channel walls

The heat flux density from the four walls is shown in Figure 12. The top and sides walls have a similar profile; about 300% of the average heat flux can be observed at the inlet section, this then reduces to 60-80 % (depending on which wall) in the middle section and then rises slightly at exit. This profile further confirms axial thermal conduction in the plate. A slightly higher heat flux can be observed from the top wall compared with the side walls; the side walls have a similar heat flux, while the bottom wall can be observed to be almost adiabatic. This indicates that thermal contact resistance between the bottom slab and the channel ribs is high; therefore, heat is transferred from only three walls. It may however be possible to have heat transferred from the four walls if channels are manufactured from methods which ensure the four walls are in good thermal contact.

It can therefore be concluded that in this design of micro-channel plates, heat transfer can be expected to occur from three walls only. The heat flux is non-uniform peripherally; however a uniform peripheral temperature can be expected on the walls transferring heat. Thermal conduction in the channel walls can modify the thermal wall boundary profile at the inlet and exit, however, the middle section of the channel can be approximated as a rectangular channel with three walls transferring heat under a H1 (constant axial wall heat flux with

constant peripheral wall temperature). This is consistent with Lee and Garimella [26] suggestion that micro-channels are best represented by H1 boundary condition. From Shah and London [21] the expected Nusselt number for fully developed flow through a channel with three sides transferring heat under H1 boundary condition ranges from 3.146 to 8.235, depending on the aspect ratio.

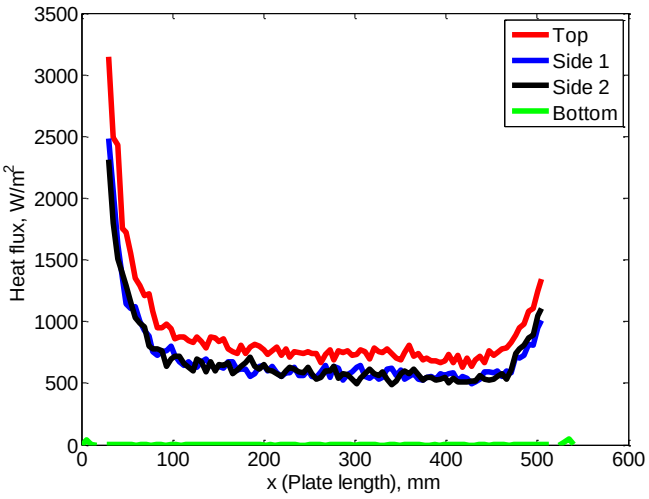

Figure 12: Heat flux profile at channel walls.

4.2 Channel efficiency (*F*)

The performance of solar collectors can be influenced both by design and operating parameters. A fraction of the solar irradiance on the collector will be reflected away and the rest will be absorbed by the plate; the magnitude of this will depend on several factors such as the glazing and surface area of the collector. However, since this study is focused on the absorber plate, only the solar irradiance absorbed by the plate q_t, will be considered. A part of this energy absorbed by the plate is further lost to the environment, the magnitude of this loss, which will vary based on several factors, can be defined in terms of an overall plate heat loss coefficient, U_L . This implies that the loss from the absorber plate can be defined as

$$q_L = U_L\left(T_p - T_a\right) \qquad (12)$$

In conventional sheet and tube solar collectors, a thermal analysis is done on the fin element. However, since this design incorporates micro-channels within the absorber plate, the fin efficiency will yield values in excess of 99.9%. A more appropriate method of obtaining the 'fin efficiency' will be to take the ratio of the thermal conduction resistance in the metal plate to the overall thermal resistance; this is referred to as the channel efficiency, '*F*'. In this analysis, the following assumptions are made.

1. The heat transfer in the flow direction is temporarily neglected.

2. Since the plate is thin and will be made of a material with good thermal conductivity, the temperature gradient through the plate (z direction) can be neglected.
3. Convection heat transfer occurs on all four sides of the channels

The thermal conduction resistance of the geometry shown in Figure 13, can be obtained using the conduction shape factor *SF*,

$$R_{cond} = \frac{1}{kSF} \tag{13}$$

The conduction shape factor for this geometry is given as [43]

$$SF = \frac{2\pi L}{0.93 \ln\left(0.948\, p/b\right)} \text{ (for } p/b > 1.41) \tag{14}$$

$$SF = \frac{2\pi L}{0.785 \ln\left(p/b\right)} \text{ (for } p/b < 1.41) \tag{15}$$

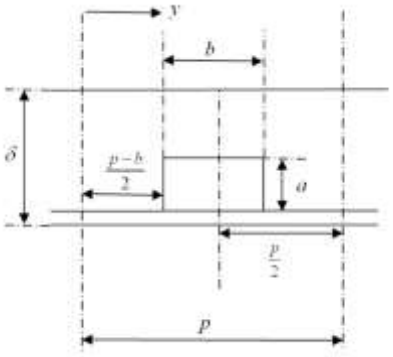

Figure 13: Dimensions on a single micro-channel

There will be a channel wall to fluid resistance when the useful energy gain, is being transferred to the thermal working fluid. It should be noted that in conventional arrangements, an additional resistance will result from the bond between tubes and sheet, hence this absorber plate design offers lesser resistance in the transfer of useful energy to the fluid. The convection resistance in a single channel can be shown to be

$$R_{conv} = \frac{1}{sh} = \frac{1}{2h(a+b)} \tag{16}$$

Figure 14 shows measured heat transfer coefficients against fluid velocities; the two plates showed a strong dependence of heat transfer coefficient on fluid velocity, this is a common phenomenon microscale heat transfer in low velocity flows. Therefore, the value of R_{conv} will vary with the fluid velocity.

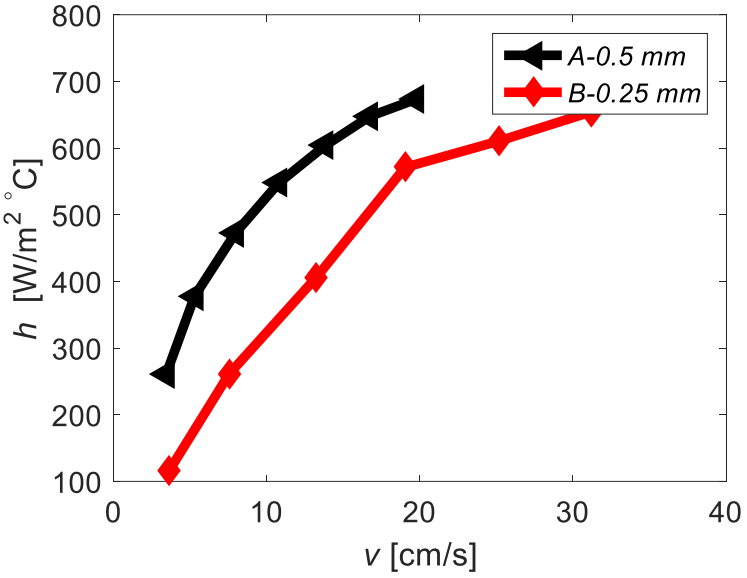

Figure 14: Heat transfer coefficient versus fluid velocity at *Pr*=21

The channel efficiency will be

$$F = \frac{R_{conv}}{R_{cond} + R_{conv}} \tag{17}$$

Figure 15 shows variation of the channel efficiency with fin length at different values of plate thermal conductivity. The figure shows that thermal conduction resistance decays as pitch distance reduces and/or thermal conductivity of the material increases. Therefore, heat loss from the absorber plate can be reduced by designing plates with channels closely spaced out.

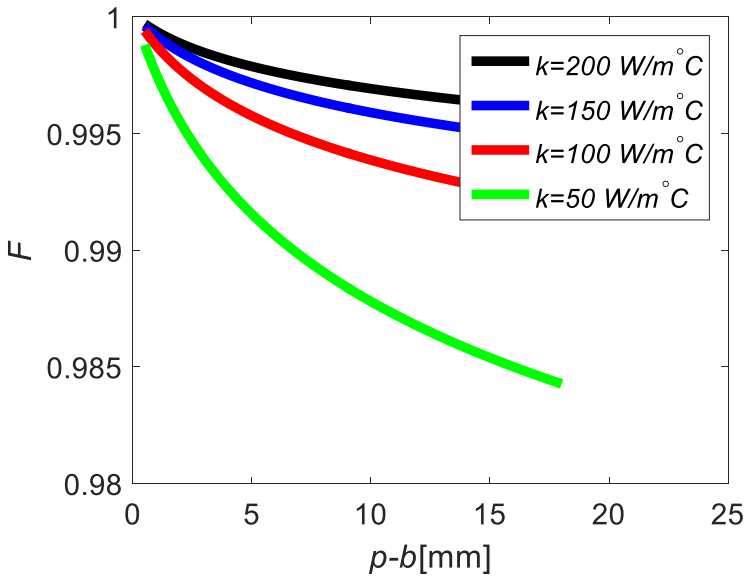

Figure 15: Fin efficiency versus fin length at h=400 W/m^2 °C

4.3 Collector Efficiency Factor (*F'*)

The collector efficiency factor F'' is defined as the ratio of the actual useful energy gain to the useful gain that would result if the collector absorbing surface was at the local fluid temperature [18].

$$F' = \frac{q_u'}{p\left[q_t - U_L\left(T_f - T_a\right)\right]} \tag{18}$$

The collector efficiency factor F' can also be defined as the ratio of the heat transfer resistance from the absorber plate to the ambient air to the heat transfer resistance from the fluid to the ambient air [18].

$$F' = \frac{1/pU_L}{\left[\frac{1}{SFk} + \frac{1}{2h(a+b)}\right]} \tag{19}$$

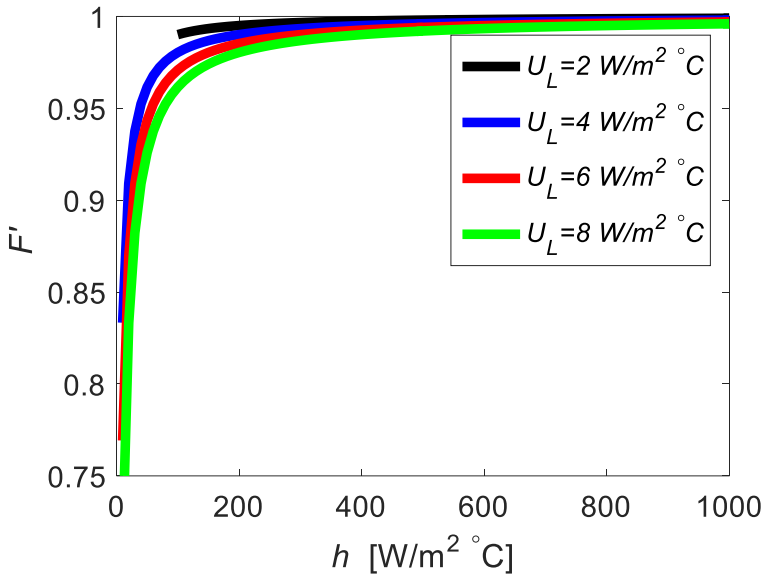

Figure 16: Collector efficiency factor versus heat transfer coefficient

Figure 16 shows a plot of the collector efficiency factor versus the heat transfer coefficient at different overall plate heat loss coefficient U_L. The range of heat transfer coefficient plotted here corresponds to experimentally measured heat transfer coefficient presented in Figure 14. It can be observed that at a particular heat loss coefficient, increasing the heat transfer coefficient above 300 W/m^2.°C results in marginal improvement of the collector efficiency factor. This is advantageous because, due to the velocity dependent heat transfer coefficient, higher heat transfer coefficient implies more pump power. Figure 17 shows how the measured heat transfer coefficient varies with the pump power measured based on pressure drop in the fluid. Figure 16 also highlights that the collector efficiency factor can be

improved by reducing the overall heat loss coefficient; this can be achieved by placing the absorber plate in a vacuum envelope such as in [44].

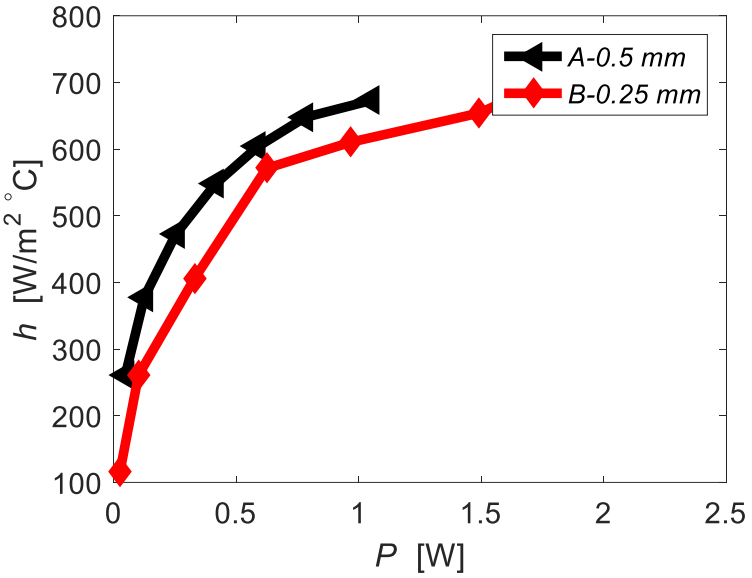

Figure 17: heat transfer coefficient versus pump power at *Pr*=21

4.4 The Heat Removal Factor (F_R)

The collector heat removal factor F_R, is a quantity that relates the actual useful energy gain of a collector to the useful gain if the whole collector surface were at the fluid inlet temperature [18]. This quantity can be evaluated by

$$F_R = \frac{\dot{m}C_p\left(T_{out} - T_{in}\right)}{A_c\left[q_t - U_L\left(T_{in} - T_a\right)\right]} \tag{20}$$

By substitution and rearrangement, F_R can also be expressed as

$$F_R = \frac{\dot{m}C_p}{A_c U_L}\left[1 - \exp\left(-\frac{A_c U_L F'}{\dot{m}C_p}\right)\right] \tag{21}$$

F_R can be observed to be similar to the effectiveness of a heat exchanger, which is the ratio of the heat transferred to the maximum possible heat that can be transferred. Therefore, the actual useful energy gain can be represented by

$$Q_u = A_c F_R\left[q_t - U_L\left(T_{in} - T_a\right)\right] \tag{22}$$

Figure 18 shows the variation of F_R with mass flow at various values of U_L and Figure 19 shows the variation of F_R with mass flow at various values of F' (F' is a function of design parameters such as *a*, *b* and *p*)

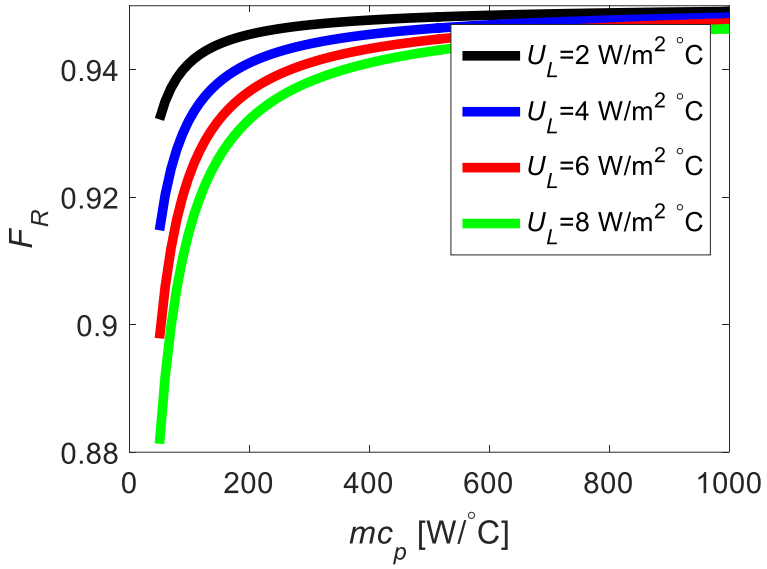

Figure 18: Heat removal factor versus mass flow rate at different U_L

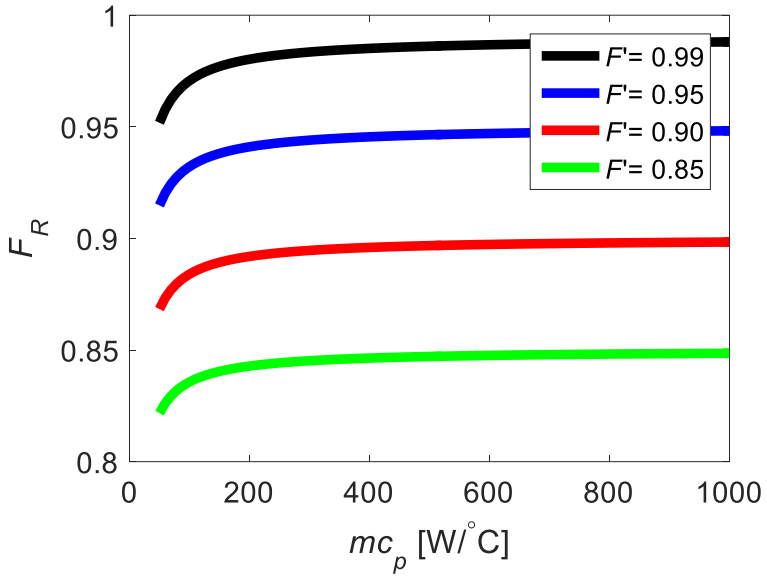

Figure 19: Heat removal factor versus mass flow rate at different F'

4.5 The Flow Factor (*F"*)

The collector flow factor *F"* is defined as the ratio of the heat removal factor to the collector efficiency factor

$$F'' = \frac{F_R}{F'} = \frac{\dot{m}C_p}{A_c U_L F'}\left[1 - \exp\left(-\frac{A_c U_L F'}{\dot{m}C_p}\right)\right] \qquad (23)$$

From equation (23), it can be observed that the flow factor is a function of a single variable which is defined as the dimensionless collector capacitance rate, CCR [18]. Where

$$CCR = \frac{\dot{m}C_p}{A_c U_L F'} \tag{24}$$

Therefore equation (23) can be written as

$$F'' = CCR\left[1 - \exp\left(-\frac{1}{CCR}\right)\right] \tag{25}$$

Figure 20 shows a plot of the flow factor as a function of the collector capacitance rate, as expected, the flow factor increases with the collector capacitance rate, therefore the collector performance can be improved by increasing the mass flow rate per collector area, $\dot{m}/A_c$, and/or reducing U_L . Higher $\dot{m}/A_c$ can be achieved by pumping the fluid at higher velocities; the increased mass flow rate then also reduces the overall collector temperature rise, albeit at the expense of increased pumping power. This will result in lower losses and increase in energy gain since the collector is at a lower temperature.

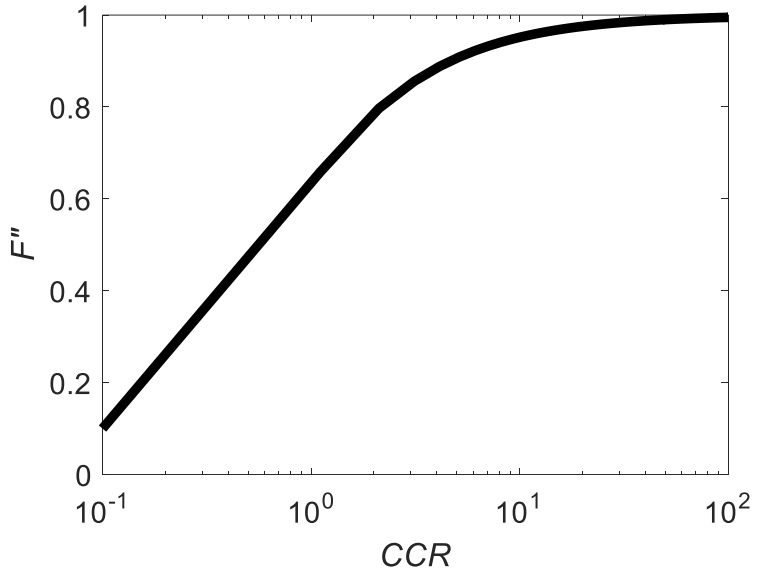

Figure 20: Collector flow factor versus collector capacitance rate

5. Conclusion

Experimental and numerical investigation into micro-channel absorber plates for compact flat plate collectors has been presented. Three-dimensional simulations using commercial CFD software, Ansys CFX, indicated that heat transfer can be expected to occur from three walls only, with a variation of the peripheral heat flux although, a uniform peripheral temperature can be expected on the walls transferring heat. Thermal conduction in the channel walls can

modify the thermal wall boundary profile at the inlet and exit, however, the middle section of the channel can be approximated as a rectangular channel with three walls transferring heat under a H1.

Standard parameters for predicting performance of the flat plate collectors have been estimated; these include channel efficiency, *F*, collector efficiency factor, *F'*, heat removal factor, F_R, flow factor *F*. An alternate parameter, channel efficiency, *F*, is proposed to replace Fin efficiency, *F* in standard collector analysis. These were evaluated over a range covering typical flat plate collector operating values; overall heat loss coefficient in the range 2 – 8 W/m^2.°C, flow rate in the range 0.01 – 0.1 kg/s/m^2 and heat transfer coefficients in the range 100 -1000 W/m^2.°C. The results showed that values of *F* and *F'* very close to unity can be achieved with this design when the overall heat loss coefficient is below 2 W/m^2.°C. The analysis further revealed that increasing the fluid-plate heat transfer coefficient beyond 300 W/m^2.°C has marginal effect on the collector efficiency factor at a given U_L value. The collector flow factor *F''* and the heat removal factor can be improved by increasing the collector capacitance rate; this can be achieved by increasing the mass flow rate per collector area $\dot{m}/A_c$, as well as reducing the overall heat loss, U_L.

Acknowledgments

This research used equipment through the Science City Energy project, part funded by the European Regional Development Fund, ERDF.

References

[1] V. Badescu, "Optimum fin geometry in flat plate solar collector systems," *Energy Conversion and Management,* vol. 47, *(15),* pp. 2397-2413, 2006.

[2] A. Kumar, R. Saini and J. Saini, "Heat and fluid flow characteristics of roughened solar air heater ducts–A review," *Renewable Energy,* vol. 47, pp. 77-94, 2012.

[3] B. Kundu, "Performance analysis and optimization of absorber plates of different geometry for a flat-plate solar collector: a comparative study," *Appl. Therm. Eng.,* vol. 22, *(9),* pp. 999-1012, 2002.

[4] D. Del Col *et al*, "Thermal performance of flat plate solar collectors with sheet-and-tube and roll-bond absorbers," *Energy,* vol. 58, pp. 258-269, 2013.

[5] W. Chun *et al*, "Effects of working fluids on the performance of a bi-directional thermodiode for solar energy utilization in buildings," *Solar Energy,* vol. 83, *(3),* pp. 409-419, 2009.

[6] A. Ordaz-Flores, O. Garcia-Valladares and V. Gomez, "Findings to improve the performance of a two-phase flat plate solar system, using acetone and methanol as working fluids," *Solar Energy,* vol. 86, *(4),* pp. 1089-1098, 2012.

[7] Z. Said *et al*, "Analyses of exergy efficiency and pumping power for a conventional flat plate solar collector using SWCNTs based nanofluid," *Energy Build.*, vol. 78, pp. 1-9, 2014.

[8] N. Benz and T. Beikircher, "High efficiency evacuated flat-plate solar collector for process steam production," *Solar Energy,* vol. 65, *(2),* pp. 111-118, 1999.

[9] K. K. Nielsen *et al*, "Degradation of the performance of microchannel heat exchangers due to flow maldistribution," *Appl. Therm. Eng.*, vol. 40, pp. 236-247, 2012.

[10] J. Vestlund, J. Dalenbäck and M. Rönnelid, "Thermal and mechanical performance of sealed, gas-filled, flat plate solar collectors," *Solar Energy,* vol. 86, *(1),* pp. 13-25, 2012.

[11] F. Davoine *et al*, "Modeling of gradient index solar selective surfaces for solar thermal applications," *Solar Energy,* vol. 91, pp. 316-326, 2013.

[12] A. G. Hestnes, "Building integration of solar energy systems," *Solar Energy,* vol. 67, *(4),* pp. 181-187, 1999.

[13] Y. Tripanagnostopoulos, M. Souliotis and T. Nousia, "Solar collectors with colored absorbers," *Solar Energy,* vol. 68, *(4),* pp. 343-356, 2000.

[14] T. Matuska and B. Sourek, "Façade solar collectors," *Solar Energy,* vol. 80, *(11),* pp. 1443-1452, 2006.

[15] M. A. Oyinlola, G. S. F. Shire and R. W. Moss, "Thermal analysis of a solar collector absorber plate with microchannels," *Exp. Therm. Fluid Sci.,* vol. 67, pp. 102-109, 10, 2015.

[16] F. Arya *et al*, "Current Developments in Flat-Plate Vacuum Solar Thermal Collectors," *World Academy of Science, Engineering and Technology, International Journal of Chemical, Molecular, Nuclear, Materials and Metallurgical Engineering,* vol. 10, *(6),* pp. 692-696, 2016.

[17] G. P. Celata, "Heat transfer and fluid flow in microchannels," *Boiling and Evaporation,* 2004.

[18] J. A. Duffie and W. A. Beckman, *Solar Engineering of Thermal Processes.* Wiley New York, 20133.

[19] M. A. Oyinlola, G. S. F. Shire and R. W. Moss, "The significance of scaling effects in a solar absorber plate with micro-channels," *Appl. Therm. Eng.*, vol. 90, pp. 499-508, 11/5, 2015.

[20] P. Rosa, T. Karayiannis and M. Collins, "Single-phase heat transfer in microchannels: the importance of scaling effects," vol. 29, pp. 3447-3468, 2009.

[21] R. K. Shah and A. L. London, *Laminar Flow Forced Convection in Ducts : A Source Book for Compact Heat Exchanger Analytical Data.* New York: Academic Press, 1978.

[22] P. Rosa, T. Karayiannis and M. Collins, "Single-phase heat transfer in microchannels: the importance of scaling effects," *Appl. Therm. Eng.*, vol. 29, *(17),* pp. 3447-3468, 2009.

[23] M. Rahimi and R. Mehryar, "Numerical study of axial heat conduction effects on the local Nusselt number at the entrance and ending regions of a circular microchannel," *International Journal of Thermal Sciences,* vol. 59, pp. 87-94, 2012.

[24] A. G. Fedorov and R. Viskanta, "Three-dimensional conjugate heat transfer in the microchannel heat sink for electronic packaging," *International Journal of Heat and Mass Transfer,* vol. 43, *(3),* pp. 399-415, 2000.

[25] G. Tunc and Y. Bayazitoglu, "Heat transfer in rectangular microchannels," *International Journal of Heat and Mass Transfer,* vol. 45, *(4),* pp. 765-773, 2002.

[26] P. Lee and S. V. Garimella, "Thermally developing flow and heat transfer in rectangular microchannels of different aspect ratios," *International Journal of Heat and Mass Transfer,* vol. 49, *(17),* pp. 3060-3067, 2006.

[27] O. Tonomura *et al*, "CFD-based optimal design of manifold in plate-fin microdevices," *Chemical Engineering Journal,* vol. 101, pp. 397-402, 2004.

[28] M. Khamis Mansour, "Thermal analysis of novel minichannel-based solar flat-plate collector," *Energy,* vol. 60, pp. 333-343, 2013.

[29] N. Sharma and G. Diaz, "Performance model of a novel evacuated-tube solar collector based on minichannels," *Solar Energy,* vol. 85, *(5),* pp. 881-890, 2011.

[30] Y. Deng *et al*, "Experimental investigation of performance for the novel flat plate solar collector with micro-channel heat pipe array (MHPA-FPC)," *Applied Thermal Engineering,* vol. 54, *(2),* pp. 440-449, 2013.

[31] R. Moss *et al*, "Optimal passage size for solar collector microchannel and tube-on-plate absorbers," *Solar Energy,* vol. 153, pp. 718-731, 2017.

[32] M. A. Oyinlola, G. S. F. Shire and R. W. Moss, "Investigating the effects of geometry in solar thermal absorber plates with micro-channels," *Int. J. Heat Mass Transfer,* vol. 90, pp. 552-560, 11, 2015.

[33] G. Gamrat, M. Favre-Marinet and D. Asendrych, "Conduction and entrance effects on laminar liquid flow and heat transfer in rectangular microchannels," *International Journal of Heat and Mass Transfer,* vol. 48, *(14),* pp. 2943-2954, 2005.

[34] P. Lee, S. V. Garimella and D. Liu, "Investigation of heat transfer in rectangular microchannels," *International Journal of Heat and Mass Transfer,* vol. 48, *(9),* pp. 1688-1704, 2005.

[35] (). *ANSYS CFX Product Overview*. Available: http://www.ansys.com/Products/Simulation+Technology/Fluid+Dynamics/Fluid+Dynamics+Products/ANSYS+CFX.

[36] C. ANSYS, "ANSYS CFX-Solver Modeling Guide," 2010.

[37] R. Qi *et al*, "Numerical simulations of LNG vapor dispersion in Brayton Fire Training Field tests with ANSYS CFX," *Journal of Hazardous Materials,* vol. 183, *(1),* pp. 51-61, 2010.

[38] S. K. Patel, D. Prasad and M. R. Ahmed, "Computational studies on the effect of geometric parameters on the performance of a solar chimney power plant," *Energy Conversion and Management,* vol. 77, pp. 424-431, 2014.

[39] T. Sultana *et al*, "Numerical and experimental study of a solar micro concentrating collector," *Solar Energy,* vol. 112, pp. 20-29, 2015.

[40] J. P. N. Bootello *et al*, "Aerodynamics of new solar parametric troughs: Two dimensional and three dimensional single module numerical analysis," *Solar Energy,* vol. 135, pp. 742-749, 2016.

[41] C. ANSYS, "ANSYS Meshing User's Guide." 2010.

[42] N. Obot, "Toward a Better Understanding of Friction and Heat/Mass Transfer in Microchannels--a Literature Review," *Microscale Thermophysical Engineering,* vol. 6, *(3),* pp. 155-173, 2002.

[43] Y. A. ├çengel, A. J. Ghajar and M. Kanoglu, *Heat and Mass Transfer Fundamentals and Applications.* New York: McGraw Hill Higher Education, 2011.

[44] P. Henshall *et al*, "Constant temperature induced stresses in evacuated enclosures for high performance flat plate solar thermal collectors," *Solar Energy,* vol. 127, pp. 250-261, 4, 2016.